International Journal of Microwave and Wireless Technologies

cambridge.org/mrf

Sparse recovery networks for target detection in OFDM-based passive radar

Zhixin Zhao[1,2], Baiming Liang[1], Yuanshuai Chen[1] and Hui-lin Zhou[1]

[1]School of Information Engineering, Nanchang University, Nanchang, Jiangxi, China and [2]Jiangxi Provincial Key Laboratory of Advanced Signal Processing and Intelligent Communications, Nanchang University, Nanchang, Jiangxi, China

Research Paper

Cite this article: Zhao Z, Liang B, Chen Y, Zhou H-l (2026) Sparse recovery networks for target detection in OFDM-based passive radar. *International Journal of Microwave and Wireless Technologies* **18**(4), 661–677. https://doi.org/10.1017/S1759078726103377

Received: 19 September 2025 UTC
Revised: 3 May 2026 UTC
Accepted: 8 May 2026 UTC
First published online: 17 June 2026 UTC

Keywords:
filters; passive radar; radar

Corresponding author: Zhixin Zhao;
Email: zhaozhixin@ncu.edu.cn

Abstract

With advances in deep learning for signal recovery based on sparse representation, this paper proposes two efficient sparse recovery (SR) networks to solve the target detection problem and generate range-Doppler maps in orthogonal frequency division multiplexing-based passive radar systems. First, by unfolding the alternating direction method of multipliers (ADMM) into a deep network with learnable parameters, a deep unfolding SR-ADMM-Net is developed, which avoids manual parameter configuration and achieves superior performance to ADMM. However, SR-ADMM-Net integrates sparsity prior information into the sparse recovery task via regularization but access only partial data domain knowledge. Therefore, this work proposes another method leveraging generative priors, which is derived from the least squares generative adversarial network (LSGAN) framework and termed SR-LSGAN. Generative priors can capture complex structural features of clutter and target signals, but their effectiveness depends on the solution space of the pre-trained generator. SR-LSGAN leverages prior distributions from the generative model and extends the solution space by dynamically fine-tuning parameters through gradient descent and internal learning, thereby improving recovery accuracy and target detection performance. Experiments on simulated and measured data demonstrate the generalizability and effectiveness of the proposed networks.

Introduction

Passive radar is a radar system that employs third-party illuminators to achieve a range of objectives, including target detection, direction-of-arrival estimation, imaging, and crowd-monitoring [1–4]. It utilizes existing communication, radio, and television signals as illuminators of opportunity (IOs) instead of dedicated transmitters, thereby reducing costs and avoiding spectrum interference. In the present era, the majority of wireless communication systems, including Digital Video Broadcasting on Terrestrial, Digital Television Terrestrial Multimedia Broadcasting, Digital Radio Mondiale (DRM), and Wi-Fi, employ orthogonal frequency division multiplexing (OFDM) signals as communication signals [5–8]. Consequently, OFDM-based passive radar systems have become a research focus.

Differing from traditional radar systems, OFDM-based passive radar systems typically extract the direct-path signal as a reference. This enables generation of the range-Doppler (RD) spectrum through two-dimensional matched filtering of reference and surveillance signals. Target detection and parameter estimation are subsequently performed on the RD spectrum using statistical methods. However, passive radar faces the challenge of strong direct-path interference and multipath clutter in the surveillance channel, which can mask weak targets in the RD map. Therefore, clutter suppression is usually necessary to eliminate the masking effect on the targets. The common processing methods incorporate adaptive clutter suppression in the spatial domain, temporal domain, or some joint domain and Matched Filter (MF) processing [9–12]. However, these techniques generally succeed in eliminating the low-Doppler portion of the surveillance signal but simultaneously ignore targets at low Doppler frequencies. In addition, the sidelobes generated by strong targets introduce spurious values in their adjoining Doppler cells, which leads to inaccurate estimates of the positions and amplitudes of weaker targets [13].

In recent years, sparse representation theory has been widely studied to address issues related to sidelobes and resolution in passive radar signal processing [14–18]. It exploits the prior knowledge of sparsity inherent in radar scenes to develop the sparse recovery (SR) model and optimally solves the SR model by incorporating sparse constraint terms to obtain sparse coefficient vectors corresponding to the complex amplitudes of the potential target signal and clutter. After generating a sparse coefficient RD spectrum, a sparse vector with the non-zero values can be directly the detections or a Constant False Alarm Rate-like processor can be designed to perform target detection [19]. In fact, it falls under the category of the convex optimization problem,

© The Author(s), 2026. Published by Cambridge University Press in association with The European Microwave Association.

termed the least absolute shrinkage and selection operator (LASSO). It is theoretically analyzed and experimentally verified that the SR-based algorithms can achieve better resolution and estimation performance than the conventional clutter suppression algorithms and MF processing algorithms for the estimation of multiple echoes from multipath, clutter, and targets [13].

Nevertheless, the efficient or accurate algorithms of the SR or convex optimization solving are also key points to consider in applications. Three main classes of SR algorithms have been widely studied and applied to the classical SR problem, including orthogonal matching pursuit [20], sparse Bayesian learning (SBL) [21], and iterative optimization algorithms that use ℓ_1-norm sparse regularization, such as the iterative soft thresholding algorithm [22], the approximate message passing [23], and the alternating direction method of multipliers (ADMM) [24], which use shrinkage thresholding function to solve the LASSO problem. In general, iterative optimization algorithms not only ensure that a globally optimal solution is obtained but are also more computationally efficient than SBL when dealing with large-scale data [25]. However, iterative optimization algorithms have three main limitations. Initially, the search process for SR solutions often requires hundreds of iterations. Secondly, parameter selection requires human intervention and different parameter choices may affect the convergence speed and recovery results. Finally, these algorithms lack generality and may require parameter readjustment when the input data undergoes alteration.

To address these challenges, deep learning methodologies have been extensively investigated, with model-driven deep unfolding networks (DUNs) [26–28] emerging as a significant approach that maps iterative optimization algorithms to DNNs by designing layers as iterations and converting algorithm parameters into learnable weights for accelerated convergence. While DUNs demonstrate superior performance in imaging radars (e.g., SAR/ISAR) [29–34], their application to passive radar is hindered by time-varying SR models due to uncontrollable IOs; this limitation is resolved by our proposed time-invariant SR model for OFDM passive radar [35], enabling the target detection framework in this paper. Furthermore, conventional DUNs rely on sparsity priors that lack discriminative power for complex signals [36], whereas generative priors (e.g., GANs [37–39]) model authentic signal distributions to outperform sparsity-based methods [40] – though their representational capabilities confine solutions to predefined ranges; consequently, we investigate both DUN solutions and generative-prior-enhanced frameworks for OFDM passive radar detection.

Overall, in this paper, two SR networks are investigated for target detection in OFDM-based passive radar. First, by integrating sparsity prior information into the SR task via regularization, and extending the iterative equations solved by the ADMM algorithm into layer-fixed DNNs with trainable parameters, an SR model-driven deep learning framework called SR-ADMM-Net is proposed, aiming to find the optimal parameters of the ADMM automatically and further accelerate the convergence process through the high fitting ability of DNNs. Second, based on the fact that more complex nonlinear structures can be revealed by utilizing prior distributions learned from generative models as constraints, another deep-learning approach based on the generative model least squares generative adversarial network (LSGAN), called SR-LSGAN, is proposed to achieve better SR performance. Different from conventional techniques reliant on a generative prior, this proposed approach calibrates the parameters of a pre-trained LSGAN through a hybrid approach integrating gradient descent and internal learning, enabling the pre-trained LSGAN to be adaptive and explore solutions beyond its original range. Furthermore, practical target detection applications of passive radar may encounter scenarios where the target intensity is much lower than clutter or entirely obscured. To further improve the detection capability of weak targets, a step-by-step estimation approach is proposed to facilitate weak target detection. In particular, the complex amplitudes of clutter, as firstly estimated from the sparse coefficients vectors generated by the network, are employed to reconstruct and mitigate clutter from the surveillance signal, and then the resultant clutter-free surveillance signal is utilized for MF with the reference signal, thereby achieving the detection of weak targets.

The remainder of this paper proceeds as follows. Section "Background" introduces the time-invariant SR model for OFDM-based passive radars. Section "SR-ADMM-Net" describes the flow of the ADMM algorithm and SR-ADMM-Net details. The proposed SR-LSGAN algorithm is introduced in Section "SR-LSGAN". Section "Measured Results" demonstrates the effectiveness of the two proposed network-based methods through numerical simulations, including the step-by-step estimation approach for weak target detection. Section "Measured Results" presents the measured experimental results. Finally, Section "Conclusion" concludes and discusses future perspectives.

Background

Signal model

A typical OFDM-based passive radar system comprises two signal channels: reference and surveillance channels. In the reference channel, the received signal may exhibit interference, such as multipath signals and noise, in addition to the direct-path signal. Generally, the direct-path signal can be reconstructed and used as the pure reference signal [41, 42].

$$x_{\mathrm{ref}}[n] = d[n] \tag{1}$$

where $d[n]$ is the complex envelope of the direct-path signal, which is composed of OFDM symbols. A complete OFDM symbol usually consists of the useful part and the cyclic prefix (CP). Following the definition of CP-OFDM waveforms, the time-domain discrete form of the transmitted CP-OFDM signal can be expressed as follows:

$$d[n] = \sum_{l=0}^{L-1} d_l[n - lN_{\mathrm{e}}] \tag{2}$$

where $N_{\mathrm{e}} = N_{\mathrm{u}} + N_{\mathrm{cp}}$ denotes the number of samples of a complete CP-OFDM symbol, consisting of the number of CP sample size N_{cp} and the number of subcarriers N_{u}. The parameter L is the total number of symbols, and $d_l(n)$ denotes the lth OFDM symbol with

$$d_l[n] = \sum_{k=0}^{N_{\mathrm{u}}-1} C_{l,k} e^{j\frac{2\pi}{N_{\mathrm{u}}}kn}, n \in [-N_{\mathrm{cp}}, N_{\mathrm{u}}] \tag{3}$$

where $C_{l,k}$ represents the complex modulation data for the kth subcarrier in the lth symbol.

The signal received from the surveillance channel generally contains direct-path interference, multipath signals, target echoes, and noise. Accordingly, the discrete form of the surveillance signal can

https://doi.org/10.1017/S1759078726103377 Published online by Cambridge University Press

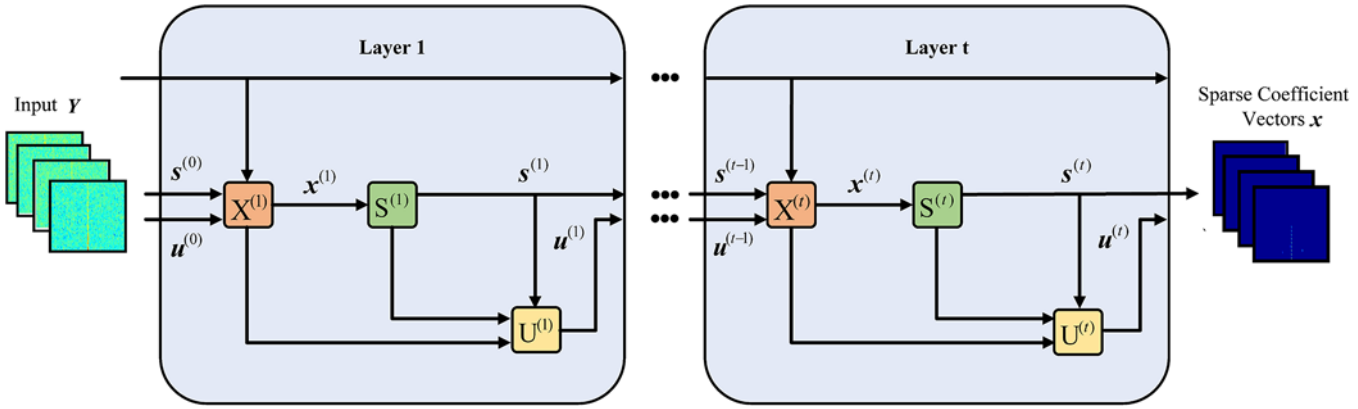


Figure 1. Data flow graph for SR-ADMM-Net.

be modeled as:

$$x_{\text{surv}}[n] = \sum_{i=0}^{N_c} c_i d[n - n_i^c] + \sum_{q=1}^{N_t} \alpha_q d[n - n_q] e^{j2\pi f_q n} + n_{\text{surv}}[n], \quad \forall n = 0, 1, \ldots, N_{\text{int}} - 1 \tag{4}$$

where c_0 and $n_0^c = 0$ denote the corresponding complex amplitude and discrete delay of the direct-path signal. Moreover, c_i and n_i^c are the complex amplitude and the discrete delay of the ith multipath echoes, respectively. α_q, n_q, and f_q are the complex amplitude, the discrete delay, and the Doppler frequency of the qth target echo, respectively. $n_{\text{surv}}[n]$ is the Gaussian white noise in the surveillance channel, and N_{int} is the number of all the discrete samples.

SR model and optimization problem for target detection

The sparsity of the echo components in passive radar can be shown in (4), which is the basis of the sparse modeling of the received data and target detection. However, it's also obvious that the received data are dependent on non-cooperative transmit waveform, resulting in many SR models and their dictionary matrices being time-varying with the transmit waveform or direct-path signal $d[n]$. A challenge of using a deep-learning network in solving the optimization problem of time-varying SR models is that pre-training a deep-learning network on a dataset generated from one particular transmit waveform may yield non-desirable performance when tested on a different transmit waveform. Specifically, the dictionary matrix of tested data pairs usually does not match the pre-training dictionary matrix due to its varying nature with the transmit waveforms and this mismatch has the potential to significantly impact the performance of the network and the rate of convergence. To address this challenge, our proposed time-invariant SR model and the associated optimization problem will be discussed next.

The idea of the time-invariant SR model is to use only the deterministically known pilots to make the dictionary matrix fixed [35]. It first performs discrete Fourier transform (DFT) on each OFDM symbol of the time-domain surveillance signal, next extracts the observation data at the pilot positions, and then performs inverse discrete Fourier transform (IDFT) on it to obtain the new time-domain surveillance signal; similarly, the transmitted data containing only the pilots are performed IDFT to the time domain as the new reference signal; and finally RD-domain data after MF are used to construct the SR model.

First, the time-domain surveillance signal, upon division into OFDM symbols, can be represented as:

$$x_{\text{surv}}[n] = \sum_{l}^{L-1} x_{\text{surv}}^l[n - lN_{\text{e}}] + n_{\text{surv}}[n] \tag{5}$$

where $x_{\text{surv}}^l[n] = \sum_{k=0}^{N_{\text{u}}-1} R_{l,k} e^{j\frac{2\pi}{N_{\text{u}}}kn}$, $n \in [-N_{\text{cp}}, N_{\text{u}}]$, $R_{l,k}$ represents the complex modulation data on the kth subcarrier in the lth symbol of the surveillance signal. Consequently, after the CPs within each symbol are removed, and the useful parts are subjected to DFT, the surveillance signal in the subcarrier domain can be represented as follows:

$$\mathbf{x}_{\text{surv_sc}} = [\mathbf{x}_{\text{surv_sc}}^0, \ldots, \mathbf{x}_{\text{surv_sc}}^l, \ldots, \mathbf{x}_{\text{surv_sc}}^{L-1}]^{\text{T}} \tag{6}$$

where $(\cdot)^{\text{T}}$ denotes the transpose, and $\mathbf{x}_{\text{surv_sc}}^l$ represent the lth symbol of the surveillance signal in the subcarrier domain, respectively, which can be expressed:

$$\mathbf{x}_{\text{surv_sc}}^l = \text{DFT}[x_{\text{surv}}^l[n]] = [R_{l,0}, R_{l,1}, \ldots, R_{l,k}, \ldots, R_{l,N_{\text{u}}-1}]^{\text{T}} \tag{7}$$

It is known that pilots are typically incorporated into OFDM waveforms for channel estimation. This allows for establishing a time-invariant SR model without needing reference signals for OFDM passive radar [35]. By keeping the complex modulation data at the pilot positions in (7) and setting the complex modulation data at the remaining positions to zero, the complex modulation data at all pilot positions in the surveillance signal within each symbol can be obtained:

$$\mathbf{x}_{\text{surv_p}}^l = [M_{l,0}, \ldots, M_{l,k}, \ldots, M_{l,N_{\text{u}}-1}]^{\text{T}} \tag{8}$$

where

$$M_{l,k} = \begin{cases} R_{l,k}, & k = p \\ 0, & \text{otherwise.} \end{cases}$$

p represents the index of the pilot within each symbol. Following the application of IDFT to the data in (8), the CPs are then incorporated into each symbol to obtain the new surveillance signal $z[n]$. Similarly, the corresponding new reference signal $v[n]$ can be generated. It should be noted that since the reference signal generated in this paper only requires pilot information and the payload data symbols are set to zero, there is no need at all to perform demodulation/remodulation processing on the reference channel signal.

https://doi.org/10.1017/S1759078726103377 Published online by Cambridge University Press

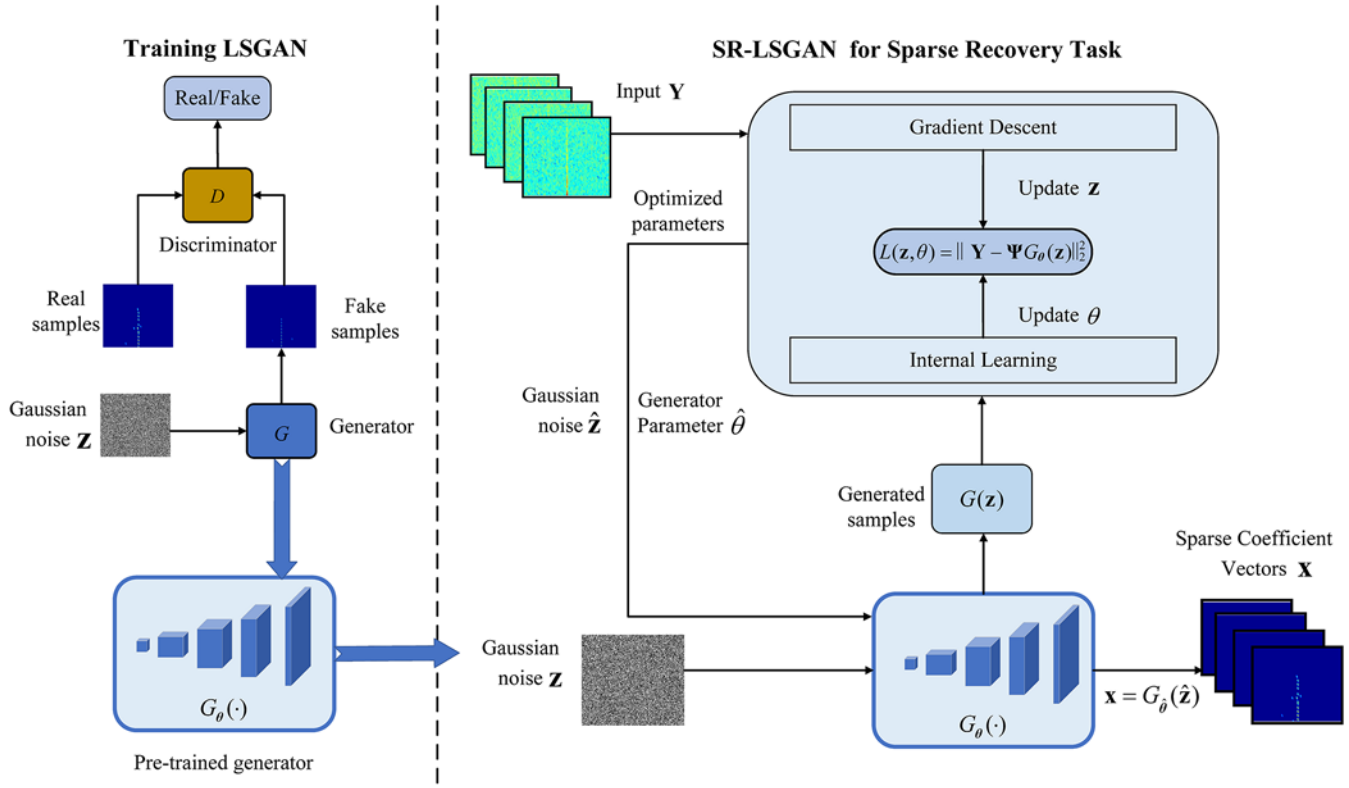


Figure 2. Overview of the proposed SR-LSGAN using deep generative priors.

In fact, there is no need to set up the reference channel anymore. According to (4), the relationship between $z[n]$ and $v[n]$ can be ascertained:

$$z[n]=\sum_{i=0}^{N_c} c_i v(n-n_i^c)+\sum_{q=1}^{N_t}\alpha_q v(n-n_q)e^{j2\pi f_q n}+\sigma[n] \tag{9}$$

where $\sigma[n]$ is the error term. By computing the cross-ambiguity function (CAF) between the new reference and surveillance signals, it becomes feasible to estimate the target information.

$$\chi[\tau,f]=\sum_{n=0}^{N_{\text{int}}-1} z[n]v^*[n-\tau]e^{-j2\pi fn/f_s} \tag{10}$$

where τ and f are the discrete delay and Doppler frequency of the target echo, respectively, f_s is the sampling frequency, and $(^*)$ stands for the conjugate. Substituting (9) into (10) yields:

$$\chi[\tau,f]=\sum_{d=1}^{N_d}\beta_d\chi_d[\tau_d,f_d] \tag{11}$$

where $N_d=N_c+N_t+1$ denotes the sum of path numbers of clutter and target echoes. $\beta_d\in[c_0,\ldots,c_{N_c},\alpha_1,\ldots,\alpha_{N_t}]$ denotes the vector of complex amplitudes of clutter and target echoes as denoted in (4). Finally, the CAF of the clutter or target echoes with discrete delay τ_d and Doppler frequency f_d can be represented as follows:

$$\chi_d[\tau,f]=\sum_{n=0}^{N_{\text{int}}-1} v[n-\tau_d]e^{j2\pi nf_d}v^*[n-\tau]e^{-j2\pi fn/f_s} \tag{12}$$

Assuming that the time delay and Doppler frequency values do not exceed $\tau_{\max}$ and $f_{\max}$, respectively, the time delay range $[0,\tau_{\max}]$ is evenly divided into L_d grids, with each grid point corresponding to a time delay value τ_i, $i=1,\ldots,L_d$. Simultaneously, the Doppler frequency range $[-f_{\max},f_{\max})$ is evenly divided into L_f grids, with each grid point corresponding to a Doppler frequency value f_j, $j=1,\ldots,L_f$. Then, the atom in the $((j-1)L_d+i)$-th column of the dictionary matrix $\mathbf{\Psi}$ can be expressed as follows:

$$\psi_{(j-1)L_d+i}=\sum_{n=0}^{N_{\text{int}}-1} v[n-\tau_i]\,e^{j2\pi nf_j}\,v^*[n-\tau]\,e^{-j2\pi fn/f_s} \tag{13}$$

It is evident that $\mathbf{\Psi}\in\mathbb{C}^{N_{\text{int}}\times J}$ is time-invariant, as it only depends on the new reference signal derived from the fixed pilot information and its dimension $J=L_dL_f$ is only related to the delay-Doppler grids. Correspondingly, the RD estimation problem for target detection becomes a SR problem as follows:

$$\mathbf{Y}=\mathbf{\Psi}\mathbf{x}+\mathbf{e} \tag{14}$$

where $\mathbf{Y}$ represents the CAF between the new reference signal and the new surveillance signal, $\mathbf{x}$ is a vectorized RD map and also a sparse coefficient vector containing the complex amplitudes of the target and clutter, and $\mathbf{e}$ is the vectorized error. Consequently, it is sufficient to estimate the non-zero component of $\mathbf{x}$ to obtain the target information. By imposing a sparsity constraint on $\mathbf{x}$ in (14), it can be transformed into the following optimization problem:

$$\min_{\mathbf{x}}||\mathbf{x}||_0 \text{ s.t. } ||\mathbf{Y}-\mathbf{\Psi}\mathbf{x}||_2^2\le\varepsilon \tag{15}$$

where $||\cdot||_b$ denotes the matrix ℓ_b-norm. Since the objective function $||\cdot||_0$ is nonconvex, the optimization problem in (15) is NP-hard, where NP stands for nondeterministic polynomial time, and thus is practically infeasible to solve optimally. One way to solve such a problem is to approximate the solution by replacing the ℓ_0-norm with the ℓ_1-norm. Thus, the above optimization problem

https://doi.org/10.1017/S1759078726103377 Published online by Cambridge University Press

Table 1. Detailed specification of LSGAN

Generator	Discriminator
Input: Noise vector $\mathbf{z}$ (1×100)	**Input:** Vector $\mathbf{x}$ (1×8000)
FC(256), Batch norm, LeakyReLU	FC(4000), LeakyReLU
FC(512), Batch norm, LeakyReLU	FC(2000), LeakyReLU
FC(1024), Batch norm, LeakyReLU	FC(512), LeakyReLU
FC(4000), Batch norm, LeakyReLU	FC(256), LeakyReLU
FC(8000), Batch norm, LeakyReLU	FC(1), LeakyReLU

is transformed into the following LASSO problem:

$$\min_{\mathbf{x}} \frac{1}{2}||\mathbf{Y} - \mathbf{\Psi x}||_2^2 + \lambda||\mathbf{x}||_1 \tag{16}$$

where $||\mathbf{Y} - \mathbf{\Psi x}||_2^2$ is a linear equation that controls the fidelity and λ is a regularization factor controlling the trade-off between fidelity and sparsity of $\mathbf{x}$.

The ADMM algorithm is an iterative optimization algorithm that is particularly effective for addressing large-scale optimization challenges, including those associated with the LASSO problem. The fundamental idea is to decompose the initial global optimization problem into a sequence of more tractable local subproblems, which usually yield closed-form solutions that can guarantee convergence to a point proximate to the optimal solution. However, the ADMM algorithm is sensitive to parameter selection, and improper parameter selection may affect the convergence speed of the algorithm and the quality of the final solution. Additionally, the computational burden associated with each iteration is considerable. As a result, researchers have turned their attention to deep learning networks.

Method

SR-ADMM-Net

The DUN represents a type of network that combines iterative optimization algorithms with deep learning architectures. The fundamental concept involves unfolding and integrating the iterative optimization algorithms into the DNN framework, capitalizing on the intrinsic parallelism of the DNN to automatically learn the optimal algorithm parameters and expedite the convergence process. This section initially derives the iterative equations pertinent to ADMM solving (16), followed by a description of the design of the SR-ADMM-Net framework.

ADMM solver

By introducing the independent auxiliary variable $\mathbf{s}$, the optimization problem in (16) can be equated to the following constrained problem:

$$\begin{aligned} &\min_{\mathbf{x},\mathbf{s}} \tfrac{1}{2}||\mathbf{Y} - \mathbf{\Psi x}||_2^2 + \lambda||\mathbf{s}||_1 \\ &\text{s.t. } \mathbf{x} - \mathbf{s} = 0 \end{aligned} \tag{17}$$

Its augmented Lagrangian function is:

$$\begin{aligned} L_\rho(\mathbf{x}, \mathbf{s}, \mathbf{u}) \quad &= \tfrac{1}{2}||\mathbf{Y} - \mathbf{\Psi x}||_2^2 + \lambda||\mathbf{s}||_1 + \\ &\tfrac{\rho}{2}||\mathbf{x} - \mathbf{s} + \mathbf{u}||_2^2 - \tfrac{\rho}{2}||\mathbf{u}||_2^2 \end{aligned} \tag{18}$$

where $\mathbf{u}$ is the Lagrange multiplier and ρ is a penalty parameter. According to the algorithm definition, the ADMM decomposes (18) into three subproblems to optimize the variables $\{\mathbf{x}, \mathbf{s}, \mathbf{u}\}$ alternately. During the tth iteration, the iterative equation is as follows:

1) $\mathbf{x}$-Update: Fix $\mathbf{s}$ and $\mathbf{u}$ to update $\mathbf{x}$; the objective function concerning the variable $\mathbf{x}$ can be articulated as follows:

$$\mathbf{x}^t = \arg\min_{\mathbf{x}} \frac{1}{2}||\mathbf{Y} - \mathbf{\Psi x}||_2^2 + \frac{\rho}{2}||\mathbf{x} - \mathbf{s}^{t-1} + \mathbf{u}^{t-1}||_2^2 \tag{19}$$

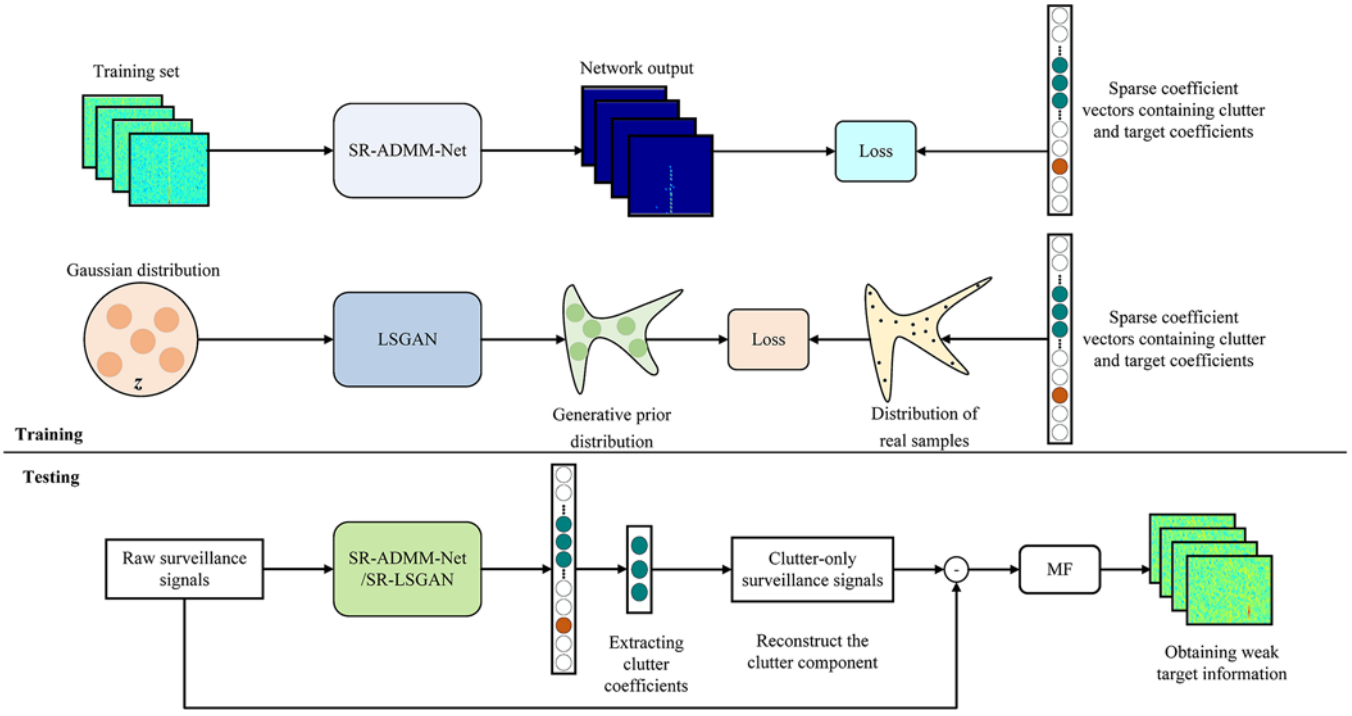


Figure 3. Step-by-step estimation approach for weak target detection.

https://doi.org/10.1017/S1759078726103377 Published online by Cambridge University Press

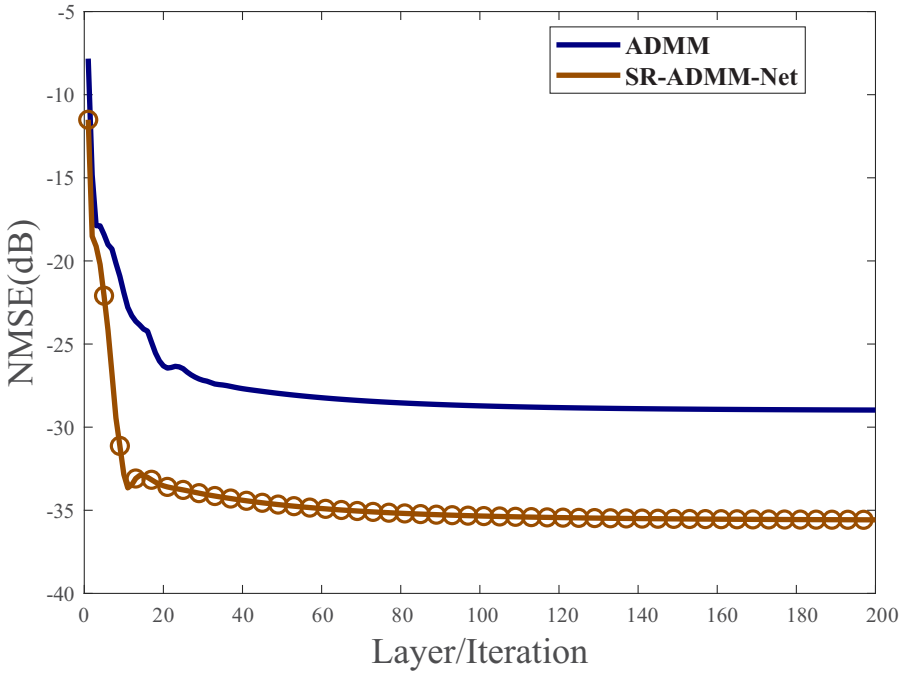


Figure 4. NMSE versus layer/iteration of SR-ADMM-Net/ADMM.

Equation (19) is essentially a ℓ_2-norm regularized least squares problem that can be solved using gradient descent.

2) **s**-Update: Fix **x** and **u** to update **s**; the objective function concerning the variable **s** can be articulated as follows:

$$\mathbf{s}^t = \underset{\mathbf{s}}{\operatorname{argmin}} \frac{\rho}{2}||\mathbf{x}^t - \mathbf{s} + \mathbf{u}^{t-1}||_2^2 + \lambda||\mathbf{s}||_1 \tag{20}$$

Equation (20) involves solving an optimization problem with ℓ_1-norm regularization that can be approximated by a soft-thresholding function, which is given as

$$\eta_\varsigma(\kappa) = \operatorname{sign}(\kappa)\max(0, |\kappa| - \varsigma) \tag{21}$$

Note that ς denotes threshold parameter, and

$$\operatorname{sign}(\kappa) = \begin{cases} \kappa/|\kappa|, \kappa \neq 0 \\ 0\,, \kappa = 0 \end{cases} \tag{22}$$

3) **u**-Update: Fix **x** and **s** to update **u**; the objective function concerning the variable **u** can be articulated as follows:

$$\mathbf{u}^t = \mathbf{u}^{t-1} + \beta(\mathbf{x}^t - \mathbf{s}^t) \tag{23}$$

where β is an update rate for the Lagrangian Multiplier.

Namely, the iterative equations for ADMM to solve (17) are

$$\begin{cases} \mathbf{x}^t = (\mathbf{\Psi}^{\mathrm{T}}\mathbf{\Psi} + \rho\mathbf{I})^{-1}(\mathbf{\Psi}^{\mathrm{T}}\mathbf{Y} + \rho(\mathbf{s}^{t-1} - \mathbf{u}^{t-1})) \\ \mathbf{s}^t = \eta_{\lambda/\rho}(\mathbf{x}^t + \mathbf{u}^{t-1}) \\ \mathbf{u}^t = \mathbf{u}^{t-1} + \beta(\mathbf{x}^t - \mathbf{s}^t) \end{cases} \tag{24}$$

where $\mathbf{I}$ is an identity matrix, and $(\cdot)^{-1}$ denotes matrix inverse.

As illustrated in (24), the ADMM algorithm necessitates a substantial amount of matrix operations, inevitably resulting in a significant computational burden. Moreover, determining the most suitable values for the parameters ρ, λ, and β in the ADMM solver poses a considerable challenge. To address these challenges, a DUN SR-ADMM-Net is developed using the iterative equations of the ADMM algorithm, wherein the tth iteration of the ADMM algorithm corresponds to the tth layer of the SR-ADMM-Net. In addition, the strong dependence of the ADMM algorithm on manual parameter selection is reduced by converting the parameters ρ, λ, and β into a series of learnable parameters, thus improving the generalization capability.

SR-ADMM-Net structure

The network structure of SR-ADMM-Net is illustrated in Figure 1, in which each layer consists of three modules: the reconstruction module $\mathbf{X}^{(t)}$, the nonlinear transform module $\mathbf{S}^{(t)}$, and the multiplier update module $\mathbf{U}^{(t)}$. Furthermore, a comprehensive description of the update procedure within SR-ADMM-Net is provided, which encompasses the formulation of the learnable parameters to facilitate rapid convergence.

Reconstruction Module $\mathbf{X}^{(t)}$: This module reconstructs the sparse coefficient vector **x** according to the reconstruction operation in (24). Given the inputs **Y**, $\mathbf{\Psi}$, and $\mathbf{s}^{(t-1)}$,$\mathbf{u}^{(t-1)}$ from layer $t-1$, the output of this module in layer t is defined as:

$$\tilde{x}^{(t)} = (\mathbf{\Psi}^{\mathrm{T}}\mathbf{\Psi} + \rho^{(t)}\mathbf{I})^{-1}(\mathbf{\Psi}^{\mathrm{T}}\mathbf{Y} + \rho^{(t)}(\tilde{s}^{(t-1)} - \tilde{u}^{(t-1)})) \tag{25}$$

where $\rho^{(t)}$ is a learnable parameter that is mainly used to control the rate of convergence. In the first layer, $\tilde{s}^{(0)}$ and $\tilde{u}^{(0)}$ are initialized to zero so that $\tilde{x}^{(1)} = \mathbf{\Psi}^{\mathrm{T}}\mathbf{Y}(\mathbf{\Psi}^{\mathrm{T}}\mathbf{\Psi} + \rho^{(1)}\mathbf{I})^{-1}$.

Nonlinear Transform Module $\mathbf{S}^{(t)}$: This module uses the soft-thresholding function defined in (21) to update **x**. Given $\mathbf{u}^{(t-1)}$ and $\mathbf{x}^{(t)}$, the output of this module in layer t is defined as:

$$\tilde{s}^{(t)} = \eta_{\varsigma^{(t)}}(\tilde{x}^{(t)} + \tilde{u}^{(t-1)}) \tag{26}$$

where $\varsigma^{(t)}$ stands for threshold, a learnable parameter determining the final convergence accuracy.

Multiplier update Module $\mathbf{U}^{(t)}$: Given the inputs $\mathbf{u}^{(t-1)}$, $\mathbf{x}^{(t)}$ and $\mathbf{s}^{(t)}$, the output of this module in layer t is defined as:

$$\tilde{u}^{(t)} = \tilde{u}^{(t-1)} + \beta^{(t)}(\tilde{x}^{(t)} - \tilde{s}^{(t)}) \tag{27}$$

Here, $\beta^{(t)}$ is a learnable parameter that controls the step size of the gradient update.

Network Parameters: In the SR-ADMM-Net framework, the learnable parameters include the step size $\rho^{(t)}$ in the reconstruction module, the shrinkage threshold $\varsigma^{(t)}$ in the nonlinear

https://doi.org/10.1017/S1759078726103377 Published online by Cambridge University Press

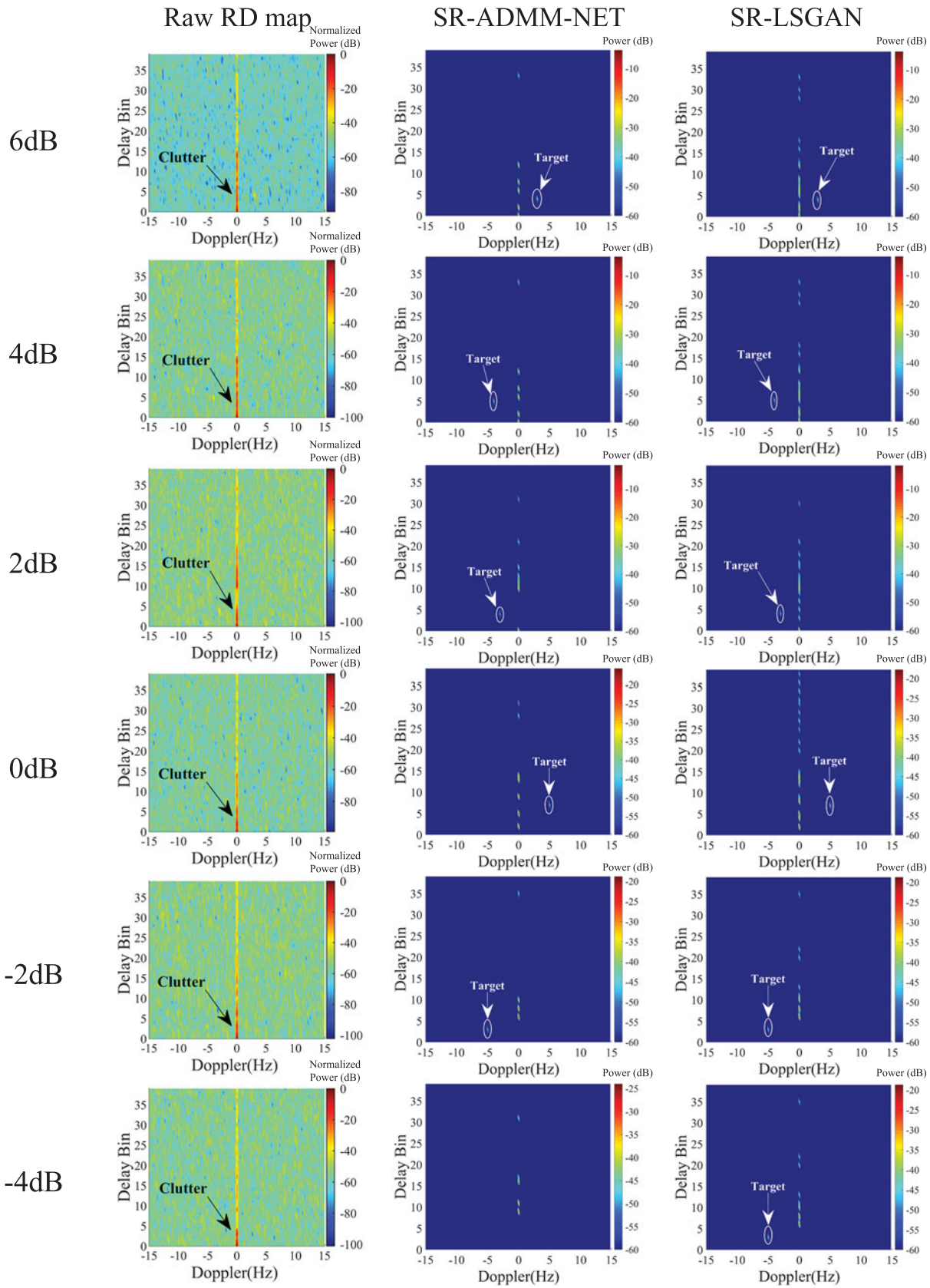


Figure 5. RD maps for one-step processing of SR-LSGAN and SR-ADMM-Net for different SNR targets.

https://doi.org/10.1017/S1759078726103377 Published online by Cambridge University Press

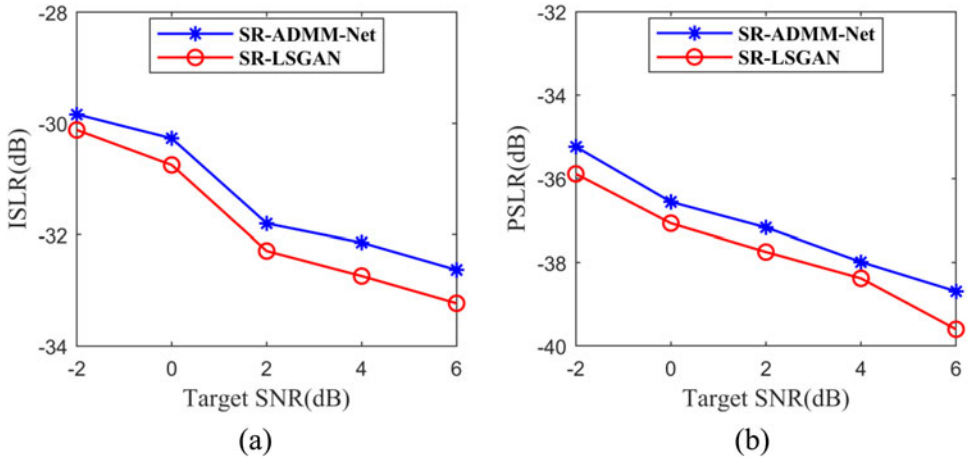


Figure 6. SR-LSGAN versus SR-ADMM-Net metric values under one-step processing with different SNR targets. (a) ISLR comparison; (b) PSLR comparison.

transformation module, and the parameter $\beta^{(t)}$ in the multiplier update module. That is, the set of learned parameters is $\Theta = \{\rho^{(1)}, \varsigma^{(1)}, \beta^{(1)}, ..., \rho^{(t)}, \varsigma^{(t)}, \beta^{(t)}\}$.

Loss function

Since an end-to-end manner is used to train the SR-ADMM-Net, the mean square error is chosen as the loss function. Given the training set Ω_{train}, the loss between the network output $\mathbf{x}^{\text{output}}$ and the ground truth $\mathbf{x}^{\text{gt}}$ is defined as:

$$Loss = \frac{1}{\Omega_{\text{train}}} \sum_{i=1}^{\Omega_{\text{train}}} ||\mathbf{x}^{\text{output}} - \mathbf{x}^{\text{gt}}||_2^2 \tag{28}$$

SR-LSGAN

The sparsity-prior-based DUN primarily relies on the judgment capacity of the ℓ_1-norm regularizer, i.e., soft-thresholding function. However, the judgment capacity of this function is limited, rendering DUN unable to capture the sparse features of the target and clutter fully. In contrast, a generative-prior-based approach can address this limitation by leveraging prior learned from a vast dataset comprising sparse coefficient vectors. However, its efficacy hinges on the solution space of the pre-trained generator. This section initially delineates the generative model LSGAN and the tenets of the generative prior-based approach. Subsequently, we propose SR-LSGAN, a novel generative-prior-based framework for passive radar target detection. Unlike conventional SR algorithms that rely on explicit ℓ_1-norm sparsity constraints, SR-LSGAN addresses the SR problem formulated in (14) by minimizing $\|\mathbf{Y} - \mathbf{\Psi} G(\mathbf{z})\|_2^2$ with $\mathbf{x} = G(\mathbf{z})$, where the generator G in the latent space implicitly learns the data distribution of the sparse coefficient samples $\mathbf{x}$.

Least squares generative adversarial network

GAN represents an implicit generative model that models the probability density function via a stochastic process directly generating data. A GAN consists of two primary components: the generator G and the discriminator D. The generator aims to learn the distribution of real samples and generate fake samples that adhere to this distribution to deceive the discriminator. The discriminator's role is to differentiate between real samples and those generated by the generator. Specifically, the generator primarily achieves a mapping from a low-dimensional latent space to a high-dimensional sample space: $\mathbf{z} \in \mathbb{R}^a \rightarrow G(\mathbf{z}) \in \mathbb{R}^b, a \ll b$. Thus, given low-dimensional noise vectors $\mathbf{z} \in \mathbb{R}^a$, the G can create samples $G(\mathbf{z}) \in \mathbb{R}^b$ that are more similar to the real samples $\mathbf{x}$. Subsequently, the discriminator evaluates the input samples and outputs a probability value $D(\mathbf{x})$ to signify the likelihood that the sample is real. During the training phase, the generative and discriminative networks continuously and alternately update, achieving a dynamic equilibrium. The minimax objective function for the original GAN can be represented as follows:

$$\begin{aligned} \min_G \max_D V_{\text{GAN}}(D, G) = {} & E_{\mathbf{x}\sim P_{\text{data}}(\mathbf{x})}[\log(D(\mathbf{x}))] \\ & + E_{\mathbf{z}\sim P_{\mathbf{z}}}[\log(1 - D(G(\mathbf{z}))] \end{aligned} \tag{29}$$

where $E[\cdot]$ denotes the average value, $P_{\text{data}}(\mathbf{x})$ represents the distribution of real samples, and $P(\mathbf{z})$ is the noise vector's distribution, usually Gaussian.

However, the function in (29) is susceptible to gradient disappearance during training, leading to the model's collapse. Therefore, to enhance the stability and quality of generation, this paper adopts the LSGAN proposed in [43]. LSGAN addresses the limitations of the original GAN by integrating the least squares loss into the adversarial loss function. The loss function of LSGAN is as follows:

$$\begin{aligned} \min_D V_{\text{LSGAN}}(D) = {} & \frac{1}{2} E_{\mathbf{x}\sim P_{\text{data}}(\mathbf{x})}[(D(\mathbf{x}) - \mu_2)^2] \\ & + \frac{1}{2} E_{\mathbf{z}\sim P_{\mathbf{z}}(\mathbf{z})}[(D(G(\mathbf{z})) - \mu_1)^2] \end{aligned} \tag{30}$$

$$\min_G V_{\text{LSGAN}}(G) = \frac{1}{2} E_{\mathbf{z}\sim P_{\mathbf{z}}(\mathbf{z})}[D(G(\mathbf{z})) - \mu_3)^2] \tag{31}$$

where μ_1, μ_2, μ_3 is a scalar label that satisfies the equation $\mu_2 - \mu_3 = 1, \mu_2 - \mu_1 = 2$ (In this paper $\mu_1 = -1, \mu_2 = 1, \mu_3 = 0$ are used).

Recovering objects using generative priors

The core concept of the generative-prior-based methodology is to leverage the prior knowledge embedded within a pre-trained generative model to address a series of linear inverse problems. Accordingly, for the linear inverse problem delineated in (14), it is sufficient to construct a large training set that encompasses a multitude of sparse coefficient vectors $\mathbf{x}$ and to train the LSGAN. At this juncture, the pre-trained generator is capable of effectively

https://doi.org/10.1017/S1759078726103377 Published online by Cambridge University Press

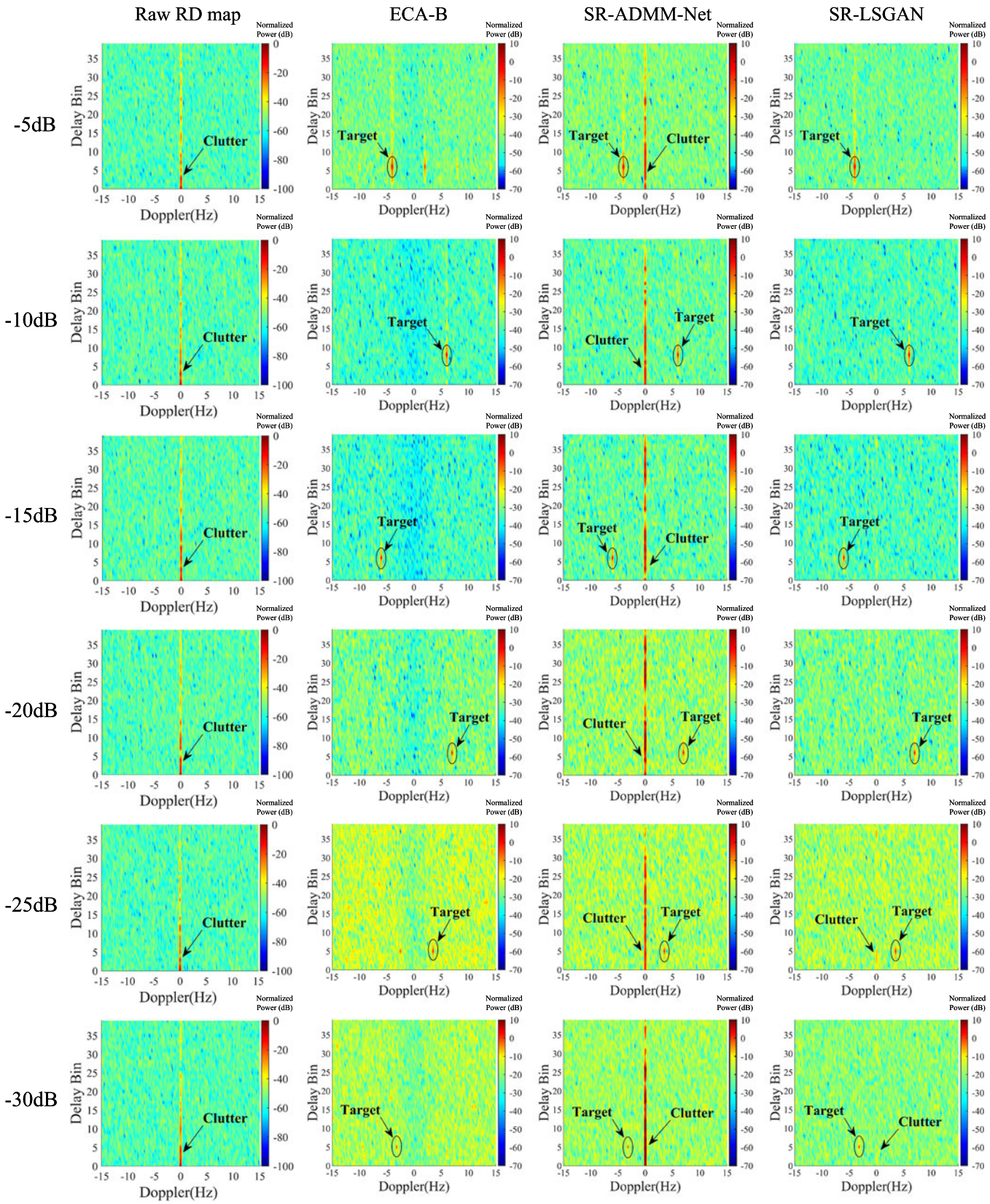


Figure 7. RD maps for step-by-step estimation for different SNR targets.

https://doi.org/10.1017/S1759078726103377 Published online by Cambridge University Press

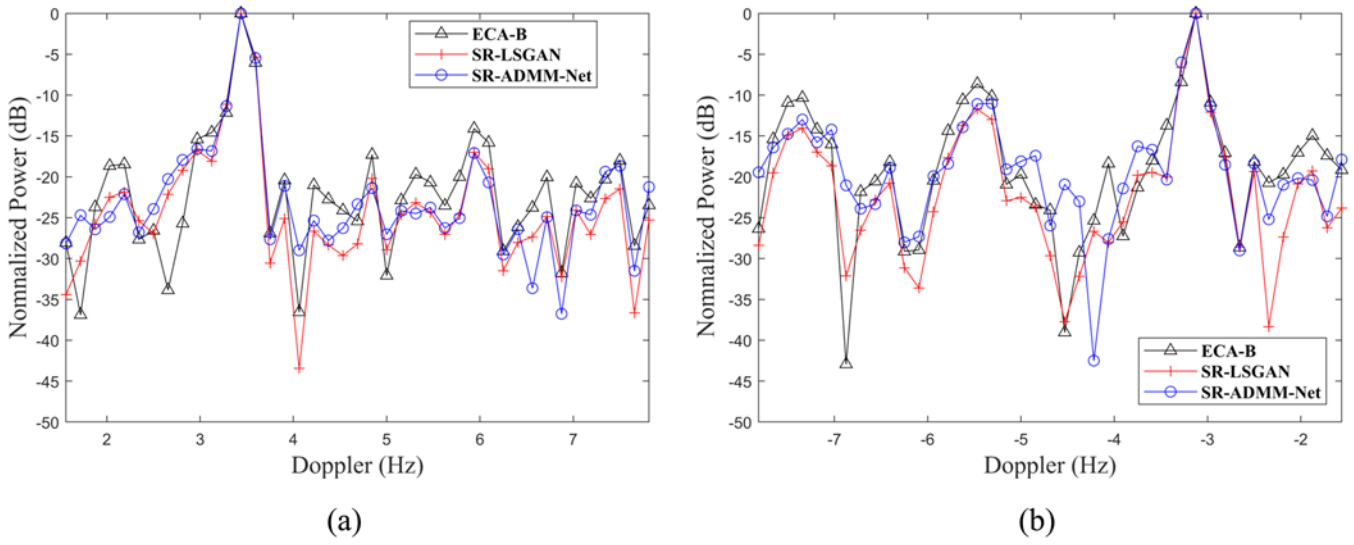


Figure 8. Normalized target range bins comparison at different SNR levels. (a) Results for −25 dB target SNR; (b) results for −30 dB target SNR.

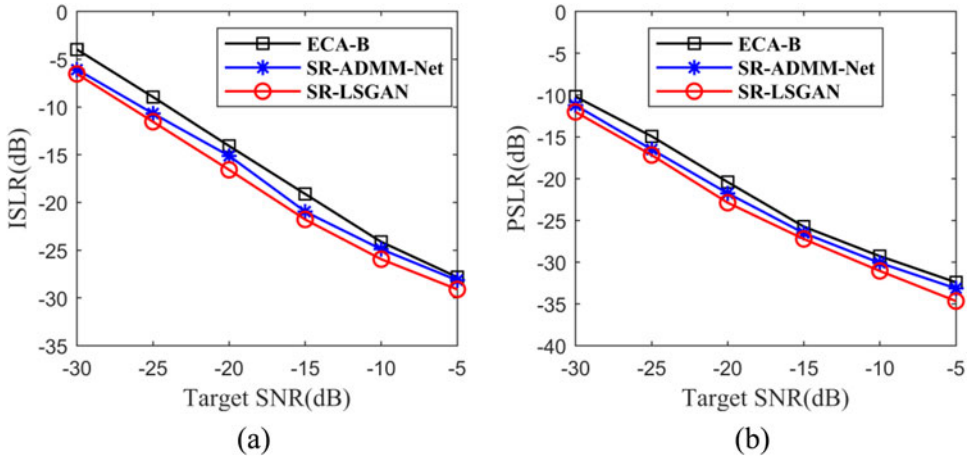


Figure 9. Values of metrics versus different target SNRs. (a) ISLR comparison; (b) PSLR comparison.

approximating the high-dimensional prior distributions associated with the set of classes to which $\mathbf{x}$ belongs (the training set) and thus can serve as an alternative prior to the sparsity prior in (14). By optimizing noise vector $\mathbf{z}$ in the solution space defined by G, an estimate $\mathbf{x}^* = G(\mathbf{z})$ of the true vector $\mathbf{x}$ is obtained. Consequently, the resolution of (14) is framed as the minimization of the following loss function:

$$L(\mathbf{z}) = ||\mathbf{Y} - \mathbf{\Psi} G(\mathbf{z})||_2^2 \tag{32}$$

This optimization procedure can be viewed as adjusting the noise vector $\mathbf{z}$ to ensure that the pre-trained generator accurately generates an estimate of the true solution vector $\mathbf{x}$. The generator G is usually differentiable, allowing for the solution of (32) using the gradient descent. However, the pre-trained generator's characterization capabilities are limited. When applying gradient descent directly to $\mathbf{z}$, the solution space is constrained to G. Moreover, if initialized improperly, the gradient descent method may converge to a local minimum, often necessitating multiple restarts to achieve optimal performance in practice [44].

SR-LSGAN algorithm for sparse recovery task

To address the challenge of restricted generator representation capacity, this paper proposes SR-LSGAN, as shown in Figure 2. This methodology enhances generator adaptability during offline training by combining gradient descent with internal learning to fine-tune the pre-trained parameters $\boldsymbol{\theta}$. Notably, unlike the conventional practice of reconstructing $\mathbf{x}$ as $G(\mathbf{z})$, our optimization simultaneously adjusts both the noise vector $\mathbf{z}$ and generator parameters $\boldsymbol{\theta}$ by minimizing the cost function:

$$L(\mathbf{z}, \boldsymbol{\theta}) = ||\mathbf{Y} - \mathbf{\Psi} G_{\boldsymbol{\theta}}(\mathbf{z})||_2^2 \tag{33}$$

The optimization of (33) can be conducted through backpropagation and the Adam optimizer. This data consistency constraint enhances the reliability of the network-generated data. Given that zero initialization outperforms random initialization, $\mathbf{z}$ is instantiated to zero in this case. Subsequently, the variables $\mathbf{z}$ and $\boldsymbol{\theta}$ are concurrently minimized to derive $\hat{\mathbf{z}}$ and $\hat{\boldsymbol{\theta}}$, and the final estimate $\mathbf{x}^*$ is given by:

$$\mathbf{x}^* = G_{\hat{\theta}}(\hat{\mathbf{z}}) \tag{34}$$

https://doi.org/10.1017/S1759078726103377 Published online by Cambridge University Press

Algorithm 1 SR-LSGAN

Input: Raw input $\mathbf{Y}$; dictionary matrix $\mathbf{\Psi}$; Iteration number T_{in}; Pre-trained generator G
Output: Sparse coefficient vector $\mathbf{x}$
Initialize $\mathbf{z} = 0$, $\boldsymbol{\theta}$
for $i = 1$ to T_{in} **do**
$\mathbf{z}_i, \boldsymbol{\theta}_i \leftarrow \underset{\mathbf{z},\boldsymbol{\theta}}{\text{argmin}} ||\mathbf{Y} - \mathbf{\Psi} G_{\boldsymbol{\theta}}(\mathbf{z})||_2^2$
end for
$\mathbf{x} \leftarrow G_{\boldsymbol{\theta}_i}(\mathbf{z}_i)$
return $\mathbf{x}$

Table 2. Parameters of the five simulated targets

Target	Delay (samples)	Doppler (Hz)	SNR (dB)
T1	3	−0.3	−2
T2	8	8	−2
T3	6	−9	−3
T4	15	0.5	−10
T5	12	6	−20

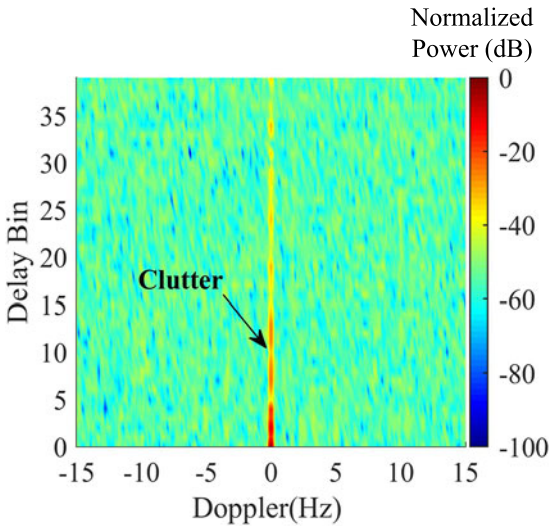


Figure 10. Raw RD map in multi-target scenarios.

$$\begin{bmatrix} \text{Re}(\mathbf{Y}) \\ \text{Im}(\mathbf{Y}) \end{bmatrix} = \begin{bmatrix} \text{Re}(\mathbf{\Psi}) & -\text{Im}(\mathbf{\Psi}) \\ \text{Im}(\mathbf{\Psi}) & \text{Re}(\mathbf{\Psi}) \end{bmatrix} \cdot \begin{bmatrix} \text{Re}(\mathbf{x}) \\ \text{Im}(\mathbf{x}) \end{bmatrix} \tag{35}$$

Results

Simulation results and analysis

Experiment settings

1) *Training Set*: In this paper, the transmit OFDM signal is generated based on DRM signals with a bandwidth of 10 KHz, 256 subcarriers, of which only 207 are valid subcarriers and a sampling frequency of 24 KHz. OFDM signals are organized in superframes, each consisting of three transmission frames, in which plum-shaped gain pilots are set for channel estimation. In the surveillance channel, 10–12 scatterers are randomly selected to simulate multipath echoes. The delays and clutter-to-noise ratios (CNRs) of the multipath are randomly determined, with the delay ranging from 0 to 40 sample intervals and the CNRs ranging from 0 to 30 dB. Additionally, the CNR of the direct-path signal is set to 40 dB, and the thermal noise is modeled as complex Gaussian white noise. Additionally, a simulated target echo with random delay and Doppler shift is included in each training set sample. The Doppler shift range of the target is from −10 to 10 Hz, the discrete delay range is from 0 to 20 sample intervals, and the signal-to-noise ratio (SNR) range of the target echo is from −30 to 10 dB. A total of 480 OFDM symbols are used to generate the training set. The delay range for the dictionary matrix is set to (0:1:40) sample intervals, the Doppler shift range is (−10:0.2:10) Hz, i.e., the total number of RD grids J is 8000, and the total number of samples of sparse coefficient vectors in the training set is 5000.

2) *Testing Set*: The parameter settings for clutter and target in the testing set are identical to those in the training set, and a total of 2000 samples are generated for the testing set.

3) *Preprocess of Complex-Value Data*: Since the passive radar data are complex-valued, it is necessary to preprocess the data to enable the general deep neural networks to deal. In this paper, given the complex-valued vectors $\mathbf{Y}$, $\mathbf{x}$ and matrices $\mathbf{\Psi}$, the matrix-vector multiplication can be decomposed and expressed as:

where Re(·) and Im(·) represent the real and imaginary components of the complex-valued data, respectively. By connecting the real and imaginary components of the vectors, reorganizing the matrix as illustrated in (35), and normalizing the data in $\mathbf{Y}$ and $\mathbf{\Psi}$, the complex-valued passive radar data can be handled by SR-ADMM-Net and SR-LSGAN.

4) *Network Configuration and Training*: In the experiment, the SR-ADMM-Net and LSGAN described in this paper were trained on a Windows 10 operating system using the PyTorch framework. The CPU of the experimental environment is a 7th generation i7-7800X running at 3.50 GHz, and the GPU is an NVIDIA GeForce RTX 2080Ti.

The SR-ADMM-Net was trained using the following hyperparameters: a batch size of 10, a learning rate of 0.001, 20 epochs, 8 network layers, and a dynamic learning rate set to decrease to 0.1 times the original value every 5 epochs to aid convergence. The initial values of the learnable parameters $\Theta = \{\rho^{(0)}, \varsigma^{(0)}, \beta^{(0)}\}$ were set to 0.05, 0.001, 1.

The structure of LSGAN is illustrated in Table 1. The generator and discriminator both comprise fully connected (FC) layers, with the dimensionality of the low-dimensional noise vector $\mathbf{z}$ set to 100. During the training process, the LSGAN was optimized using the Adam optimizer with the following hyperparameters: the generator's learning rate was set to 0.0001, the discriminator's learning rate was set to 0.00005, the batch size was 100 and 400 epochs of training. In algorithm 1, the optimization procedure in (33) was solved by using the Adam optimizer, the number of iterations was set to 5000, and the learning rate of both $\mathbf{z}$ and $\boldsymbol{\theta}$ was 0.0001.

5) *Step-by-Step Estimation Approach for Weak Target Detection*: As shown in Figure 1 and 2, the network output is the sparse coefficient vectors equal to the vectorized RD maps. Consequently, it is possible to directly obtain the coefficient vectors corresponding to the multiple echo components, including clutter and target echoes, following the acquisition of the network output during the testing phase. However, in the field of OFDM passive radar, there are

https://doi.org/10.1017/S1759078726103377 Published online by Cambridge University Press

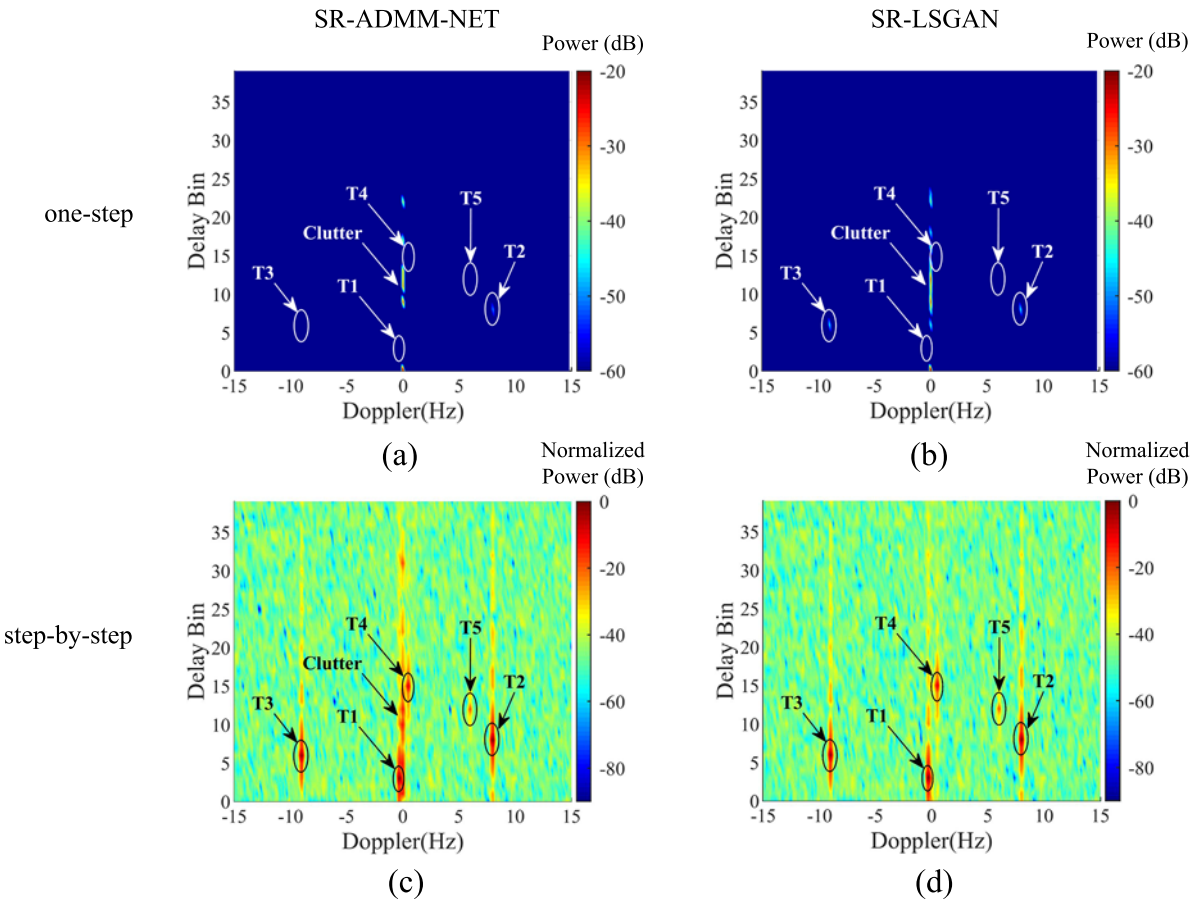


Figure 11. RD maps in multi-target scenarios. (a) SR-ADMM-Net with one-step; (b) SR-LSGAN with one-step; (c) SR-ADMM-Net with step-by-step; (d) SR-LSGAN with step-by-step.



Figure 12. Experiment layout of DRM-based OFDM passive radar.

many instances where the target signal is exceedingly weak, with an intensity thousands of times lower than that of the direct-path signal, and it may be totally masked by clutter. In these scenarios, the network may struggle to simultaneously effectively learn the sparse features of the weak target and strong clutter or by one-step processing, which makes the network's output, vectorized RD maps, produce several false targets caused by noise, potentially resulting in misidentification of the actual target.

https://doi.org/10.1017/S1759078726103377 Published online by Cambridge University Press

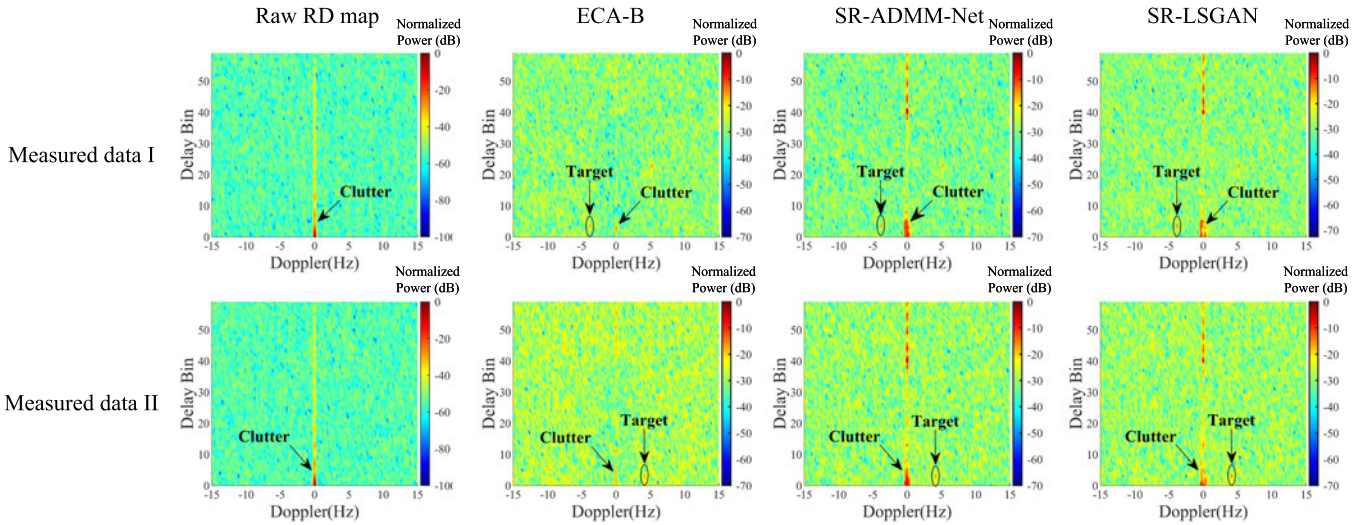


Figure 13. RD maps of measured data I and II.

Thus, to detect as many weak targets as possible, a step-by-step estimation approach is used as outlined below: after obtaining the sparse coefficient vectors of the network output, the clutter coefficients in the sparse coefficient vectors are extracted to create a clutter-only surveillance signal. It is easy to distinguish the sparse coefficients of clutter because they generally occur near the zero-Doppler frequency of the RD map and usually with stronger intensity. Subsequently, the clutter component is subtracted from the initial surveillance signal by the CLEAN algorithm [45]. Finally, the resulting signal is match-filtered with the reference signal, thereby enabling the detection of weak targets. The proposed step-by-step estimation approach is illustrated in Figure 3.

Results and analysis

1) *Simulation 1: Convergence Speed of SR-ADMM-Net vs. ADMM*: As stated before, SR-ADMM-Net is proposed to automatically learn the optimal parameters and accelerate the convergence process of ADMM. So, the convergence speeds of SR-ADMM-Net with ADMM will be analyzed in this part. To compare the convergence speed of SR-ADMM-Net with ADMM, the average normalized mean square error (NMSE) calculated on the test set of both methods is utilized for assessment. NMSE in dB scale is defined as:

$$\mathrm{NMSE} = 10\log_{10}\Big[\frac{1}{\Omega_{\mathrm{test}}}\sum_{i=1}^{\Omega_{\mathrm{test}}}\frac{||\mathbf{x}^{\mathrm{gt}}-\mathbf{x}^{\mathrm{output}}||_2^2}{||\mathbf{x}^{\mathrm{gt}}||_2^2}\Big] \tag{36}$$

The iterative equations of the ADMM algorithm are given by (24), and the setting of the parameters in its algorithm is consistent with the initialization parameters of SR-ADMM-Net. Figure 4 shows NMSE values versus the number of network layers of the SR-ADMM-Net and the number of iterations of the ADMM algorithm under the testing set. The findings indicate that the proposed SR-ADMM-Net achieves an NMSE value of about −28 dB with only about eight layers. In comparison, traditional ADMM requires more than 50 iterations to reach a final similar convergence value. Moreover, the final convergence value of SR-ADMM-Net can further drop to −35dB. These results confirm that SR-ADMM-Net achieves a faster convergence rate and higher accuracy through the automatic learning of parameters.

2) *Performance Assessment*: To provide a quantitative evaluation of the target detection performance of the proposed networks, two metrics, namely the peak-to-sidelobe level ratio (PSLR) and the integrated-sidelobe level ratio (ISLR), are employed in the simulation experiments [46]. PSLR denotes the ratio between the highest sidelobe and the peak value, which reflects the radar's ability to detect weak targets. PSLR in dB scale is defined as:

$$\mathrm{PSLR} = 20\log(\max_{\omega\in Q,\nu\in F}(|\psi[\omega,\nu]|)/\psi[\omega_0,\nu_0]) \tag{37}$$

where ψ denotes the estimated RD map, ω_0 and ν_0 denote the range bin and Doppler bin of target, respectively. The parameters Q and F define the set of range bins and Doppler bins in the RD map in addition to the main lobe. The ISLR is the ratio between the energy accumulation of the sidelobes and the peak value, which measures the energy distributed in the sidelobes. ISLR in dB scale is defined as:

$$\mathrm{ISLR} = 10\log((\sum_{\omega\in Q,\nu\in F}|\psi[\omega,\nu]|^2)/(\sum_{\omega\in Q,\nu\notin F}|\psi[\omega,\nu]|^2)) \tag{38}$$

Therefore, lower PSLR and ISLR values represent better performance.

3) *Simulation 2: Comparison of One-step Processing Results Between SR-ADMM-Net and SR-LSGAN*: To accurately analyze the sparse coefficient estimation capability of SR-ADMM-Net and SR-LSGAN, samples with relatively high target SNRs ranging from 6 dB to −4 dB, with the step of 2 dB, have been selected from the test set for the simulation experiments. Additionally, the sparse component coefficients present in the echoes are directly output for target detection through the one-step processing approach depicted in Figures 1 and 2.

Figure 5 presents the simulation results obtained from vectorized RD maps across different target SNRs, directly produced by SR-ADMM-Net and SR-LSGAN. The raw RD maps without clutter suppression are normalized via individual maximum normalization. The findings indicate that at higher target SNRs, the network's output enables direct identification of the target and clutter. However, it is noticeable that the SR-ADMM-Net struggles to identify the target when the target SNR falls below −2 dB. This limitation is attributed to the constrained discriminative ability of the sparsity prior, which does not adequately capture the sparse feature of the target. In contrast, the SR-LSGAN, which is based on generative prior, not only successfully identifies the target but also

https://doi.org/10.1017/S1759078726103377 Published online by Cambridge University Press

effectively estimates all clutter paths. Consequently, the capability for sparse feature extraction about both clutter and the target of SR-LSGAN is superior to that of SR-ADMM-Net.

To further evaluate the target detection performance of the two methods under a one-step estimation approach, 100 Monte Carlo simulations were conducted using the test set data during the simulation experiments to calculate each metric. Figure 6 illustrates the performance curves of the metric values for the two methodologies of different target SNRs, it can be observed that the discrepancy between the metric values of the two methods is relatively minor when both methods are capable of detecting the target. At this juncture, the PSLR and ISLR values of the SR-LSGAN are approximately 0.5 dB lower than those of the SR-ADMM-Net. However, as the target SNR is progressively diminished, the SR-LSGAN maintains its capability to detect the target. Consequently, it can be concluded that the target detection performance of SR-LSGAN is markedly superior to that of SR-ADMM-Net when employing the one-step processing approach.

4) *Simulation 3: Comparison of Step-by-Step Estimation Results*: This subsection will further analyze the detection capabilities of SR-ADMM-Net and SR-LSGAN in identifying weak targets under the step-by-step estimation approach through simulation experiments. Additionally, the performance of both methods will be compared to that of the commonly used clutter suppression algorithm, ECA-B [12]. To ensure a fair and physically meaningful comparison, the RD maps with clutter suppression by ECA-B, SR-ADMM-net, and SR-LSGAN are processed with target peak normalization.

Figure 7 illustrates the simulation results of the three methods under different target SNRs, where the ECA-B algorithm is configured with 40 blocks, each containing a signal length of 4000. It is evident that the target signal is obscured within the clutter sidelobes without clutter suppression due to the direct-path signal and multipath clutter interference, making it challenging to detect. As shown in Figure 7, although SR-ADMM-Net can detect a target, some residual clutter remains, and target detection becomes increasingly challenging when the target SNR is degraded. In contrast, the SR-LSGAN and ECA-B algorithms effectively eliminated the influence of clutter, enabling clear observation of the target. However, due to the chunking process, the ECA-B algorithm may introduce blurred sub-peaks.

Figure 8 shows the normalized target-range bin cuts after clutter suppression at target SNRs of −25 dB and −30 dB for a more direct comparison. The findings indicate that both the SR-ADMM-Net and SR-LSGAN exhibit lower noise levels compared to the ECA-B algorithm, which are attributed to the generation of some ambiguous sub-peaks by the ECA-B algorithm. Furthermore, the noise levels associated with SR-LSGAN is marginally lower than that of SR-ADMM-Net, and SR-LSGAN demonstrates superior efficacy in filtering out clutter, effectively suppressing all or most clutter at zero frequency. Consequently, SR-LSGAN is characterized by enhanced target detection capabilities.

Figure 9 illustrates the metric values associated with three methodologies across different target SNRs. The results indicate that both the PSLR and ISLR values of the proposed SR-ADMM-Net and SR-LSGAN are lower than those of the ECA-B algorithm, with SR-LSGAN achieving the lowest values, both approximately 2 dB below those of the ECA-B algorithm. Additionally, the PSLR and ISLR values for SR-LSGAN and SR-ADMM-Net do not differ significantly when the target SNR falls below −25 dB, which is because when the target SNR is low to a certain extent, the base of the RD map is no longer determined by the clutter sidelobe after clutter filtering, but by the noise component, resulting in no significant change in these two metrics. However, Within the target SNR range of −5 dB to −25 dB, SR-LSGAN demonstrates superior clutter filtering capabilities, with its PSLR and ISLR values being 1 dB lower than those of SR-ADMM-Net, in line with the results in the one-step processing approach. Furthermore, the observed inverse relationship between PSLR and ISLR concerning the target SNRs is consistent with the definitions of these metrics, thereby justifying the validity of the results.

Table 3. Metric values under the two groups of measured data

Measured data	Method	PSLR (dB)	ISLR (dB)
Measured data I	ECA-B	−7.53	−2.22
	SR-ADMM-Net	−8.38	−3.57
	SR-LSGAN	−8.66	−4.01
Measured data II	ECA-B	−6.97	−2.54
	SR-ADMM-Net	−8.13	−4.26
	SR-LSGAN	−8.70	−4.41

5) *Simulation 4: Performance Comparison of Different Methods in Multi-Target Scenarios*: A multi-target scenario experiment is performed to assess the proposed algorithms' capabilities in sparse coefficient estimation, weak target detection, and low-Doppler target detection. It contains five targets with different SNRs and RD parameters as listed in Table 2. Specifically, T1 is a target with low-Doppler frequency and relatively high SNR −2 dB, T2 is a target with the same SNR as T1 but higher Doppler frequency, T3 is a target with relatively high Doppler frequency and relatively high SNR −3 dB, T4 is a weaker target with low Doppler frequency and SNR −10 dB, and T5 is an extremely weak target with SNR −20 dB and high Doppler frequency.

It can be seen that all five targets are masked by clutter in the raw RD map in Figure 10. Figure 11 presents the RD maps after one-step and step-by-step target detection using SR-ADMM-Net and SR-LSGAN networks. After one-step processing of the proposed networks, only T2 and strong clutter are estimated by SR-ADMM-Net in Figure 11(a), while T2, T3, and more clutter are estimated by SR-LSGAN in Figure 11(b). These results demonstrate the sparse coefficient estimation capability of both networks, with SR-LSGAN outperforming SR-ADMM-Net.

To identify T1 with low-Doppler frequency, T4 with weaker SNR and low-Doppler frequency, and T5 with extremely weak SNR, step-by-step processing results of SR-ADMM-Net and SR-LSGAN are given in Figure 11(c) and (d), respectively. All five targets are clearly visible on both RD maps, demonstrating their weak target and low-Doppler target detection capabilities. Moreover, the SR-LSGAN network achieves optimal clutter suppression performance after step-by-step processing, while the sidelobes of T1 overlap with residual clutter in the SR-ADMM-Net result.

Measured results

To further demonstrate the effectiveness and superiority of the proposed method, relevant experiments are conducted using the measured data. The dataset originates from a DRM-based passive radar detection experiment, wherein the radar system receives DRM signals with an effective bandwidth of 9.7 KHz and an operating frequency of 10 MHz. The configuration of the experiment is depicted in Figure 12, with the transmitting station located off

https://doi.org/10.1017/S1759078726103377 Published online by Cambridge University Press

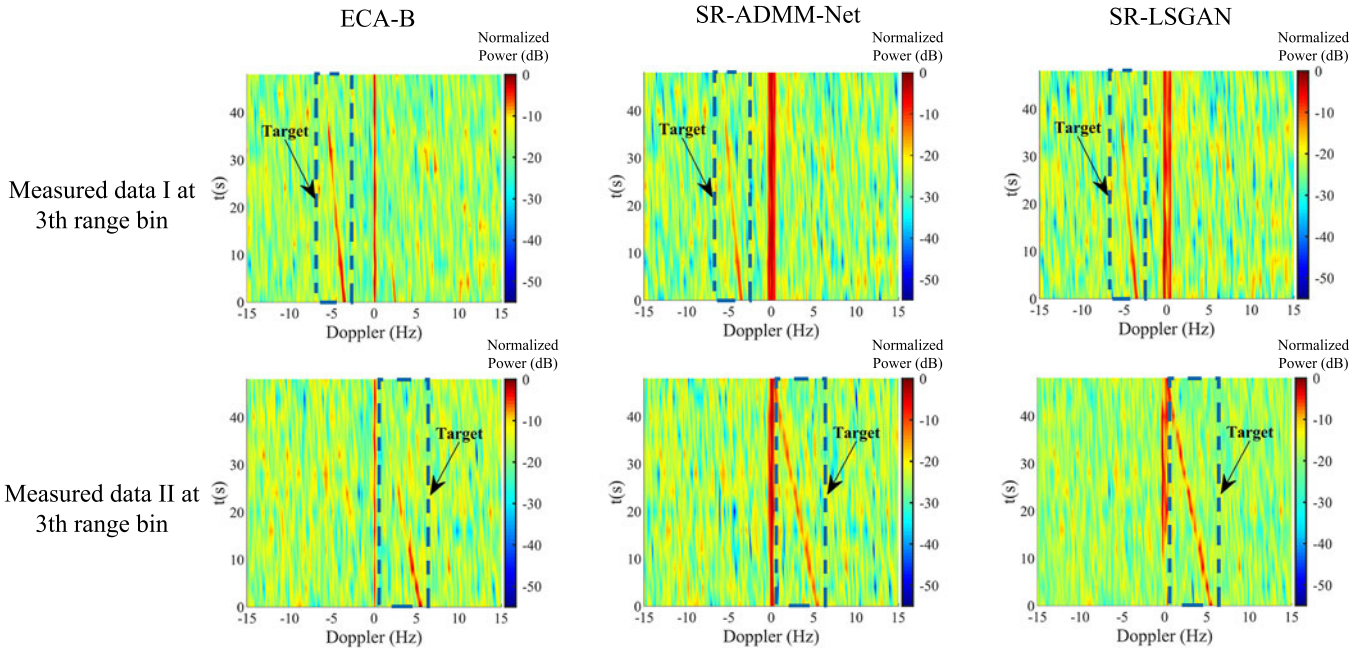


Figure 14. Trajectory maps of the targets for the two measured data sets.

the coast of Qingdao City, Shandong Province, China, and the receiving station located off the coast of Haiyang City, Shandong Province, China, approximately 50 km apart. And the receiving station was composed of a 16-element linear array.

The processing steps for the measured data are as follows: firstly, the 16-element linear receiving array is oriented toward the transmitter direction and expected target directions to capture the reference and surveillance channel signals, respectively. Then, the measured test set samples for the networks are constructed based on processing them as presented in the signal models of Section II. Given the exceedingly low SNR of the targets within the measured data, the step-by-step estimation approach is employed for target detection, and a total of 512 OFDM symbols are used for MF to generate the RD map.

Figure 13 illustrates two distinct sets of single-field measured data experiments. As the targets in the measured data are all relatively weak, they are entirely obscured by clutter in the RD map before clutter suppression. All three methods demonstrated the capacity to effectively detect the two targets with Doppler frequencies of −3.75 Hz and 4.06 Hz after clutter suppression. Additionally, Table 3 presents the PSLR and ISLR values for the two sets of measured data. The results indicate that the PSLR and ISLR values for the SR-ADMM-Net and SR-LSGAN are lower than those associated with the ECA-B algorithm, with SR-LSGAN exhibiting the lowest PSLR and ISLR values. This finding aligns with the simulation results, indicating that the proposed two SR networks exhibit superior target detection performance compared to the ECA-B algorithm.

To further demonstrate the capability and effectiveness of the proposed networks in the application of target detection in real data, the detection results of multi-field data for the same target are also analyzed, where the consecutive multi-field RD maps and the trajectory results at the target range bin are presented. The trajectory results of the target range bin are obtained by repeating the target parameter estimation for consecutive multi-field data and displaying all the results in a single map. The consecutive multi-field RD maps over 1 minute are analyzed and the interval between two adjacent fields is 4 s. The final trajectory maps for the targets from both groups of measured data are presented in Figure 14. It is evident that SR-LSGAN and SR-ADMM-Net generate more distinct and precise trajectory maps than those of the ECA-B algorithm, particularly for measured data II, which demonstrates the versatility and superiority of the two networks in practical applications.

Based on these results, subsequent estimation of parameters such as target acceleration can be further performed. However, since only the bistatic range and Doppler information of targets can be estimated from the RD spectrum, obtaining the true three-dimensional acceleration vector requires accurate calculation combined with azimuth information in subsequent processing. Notably, the network algorithm proposed in this paper preserves the phase information of the data, which can support such subsequent processing.

Conclusions

In this paper, the problem of SR for target detection in OFDM-based passive radar is investigated. Considering that the traditional iterative optimization algorithm faces challenges in selecting suitable parameters and exhibits a slow convergence rate, two SR networks, SR-ADMM-Net and SR-LSGAN, were proposed in this paper to enhance efficiency and accuracy, which utilize sparsity of data to be recovered and prior distributions learned from generative models as constraints respectively. Moreover, the one-step processing approach, which involves directly using the sparse component coefficients derived from the network output to ascertain the parameter information of the target, may result in inaccurate estimations in contexts where the target is totally masked by clutter. Consequently, a step-by-step estimation approach is proposed for detecting weak targets. Extensive experimental findings indicate that the SR-ADMM-Net demonstrates both more rapid convergence and enhanced accuracy in comparison to the ADMM

https://doi.org/10.1017/S1759078726103377 Published online by Cambridge University Press

algorithm. Furthermore, the proposed network exhibits lower PSLR and ISLR values relative to the ECA-B algorithm, suggesting that the target detection capabilities of both SR-ADMM-Net and SR-LSGAN surpass those of the ECA-B algorithm. Notably, the target detection performance of SR-LSGAN is marginally superior to that of SR-ADMM-Net. Finally, the measured data further confirmed the effectiveness and generality of our proposed networks.

Acknowledgements. This work was supported in part by the National Natural Science Foundation of China under Grants 62261036, and in part by the Natural Science Foundation of Jiangxi Province under Grants 20242BAB23010.

Competing interests. The authors report no conflict of interest.

References

1. **Zhang C, Shi S, Yan S and Gong J** (2023) Moving target detection and parameter estimation using BeiDou GEO satellites-based passive radar with short-time integration. *IEEE Journal of Selected Topics in Applied Earth Observations and Remote Sensing* **16**, 3959–3972.
2. **He Z, Yang Y, Chen W, Cao N and Guo Y** (2024) Maritime ship joint detection and localization using GNSS-based passive multistatic radar. *IEEE Transactions on Instrumentation and Measurement* **73**, 1–14.
3. **Wang P, Zhou X, Fang Y, Zeng H and Chen J** (2023) GNSS-based passive inverse SAR imaging. *IEEE Journal of Selected Topics in Applied Earth Observations and Remote Sensing* **16**, 508–521.
4. **Storrer L, Yildirim HC, Willame M, Pocoma Copa EI, Cakoni D, Pollin S, Louveaux J, De Doncker P and Horlin F** (2024) Large-scale crowd size classification with a Wi-Fi-based passive radar. *IEEE Sensors Journal* **24**, 33560–33572.
5. **Hu S, Yi J, Wan X, Cheng F, Hu Y and Hao C** (2023) Illuminator of opportunity localization for digital broadcast-based passive radar in moving platforms. *IEEE Transactions on Aerospace and Electronic Systems* **59**, 3539–3549.
6. **Zhang W, Cheng F, Wan X, Shen J and Yi J** (2024) A method to enhance the calibration performance of passive radar arrays in DTMB signal environment. *IEEE Antennas and Wireless Propagation Letters* **23**, 2556–2560.
7. **Huang D, Wang R, Zhu Q, Bai L, Zhou H and Tian Y** (2024) Nonstationary target detection using time-frequency multisqueezing transform for DRM-based passive radar. *IEEE Geoscience and Remote Sensing Letters* **21**, 1–5.
8. **Li W, Bocus MJ, Tang C, Piechocki RJ, Woodbridge K and Chetty K** (2022) On CSI and passive Wi-Fi radar for opportunistic physical activity recognition. *IEEE Transactions on Wireless Communications* **21**, 607–620.
9. **Sun Q, Shan T, Feng Y, He S, Bai X and Zhang H** (2024) A frequency domain clutter suppression approach for passive radar. *IEEE Sensors Journal* **24**, 14916–14929.
10. **Zuo L, Wang J, Sui J and Li N** (2021) An inter-subband processing algorithm for complex clutter suppression in passive bistatic radar. *Remote Sensing* **13**, 4954.
11. **Sui J, Wang J, Gao J and Fan X** (2024) An extensive cancellation algorithm via overlapping subband for time-varying clutter suppression in passive bistatic radar. *IEEE Transactions on Aerospace and Electronic Systems* **60**, 5169–5185.
12. **Colone F, O'Hagan DW, Lombardo P and Baker CJ** (2009) A multistage processing algorithm for disturbance removal and target detection in passive bistatic radar. *IEEE Transactions on Aerospace and Electronic Systems* **45**, 698–722.
13. **Feng W, Friedt J-M, Cherniak G and Sato M** (2019) Batch compressive sensing for passive radar range-Doppler map generation. *IEEE Transactions on Aerospace and Electronic Systems* **55**, 3090–3102.
14. **Zheng L and Wang X** (2017) Super-resolution delay-Doppler estimation for OFDM passive radar. *IEEE Transactions on Signal Processing* **65**, 2197–2210.
15. **Lai H, Ye K, Sun H and Hong S** (2024) Atomic norm-based joint delay-Doppler shift estimation for OFDM passive radar. *IEEE Signal Processing Letters* **31**, 36–40.
16. **Nikaein H, Zefreh RG and Gazor S** (2023) Target detection and interference cancellation in passive radar sensors via group-sparse regression. *IEEE Sensors Journal* **23**, 21484–21492.
17. **Wang X and Zhang Z** (2022) Joint range and velocity estimation for orthogonal frequency division multiplexing-based high-speed integrated radar and communications system. *IET Communications* **16**, 1005–1019.
18. **Zhao Z, Gong Y, Zhou H and Cao Y** (2024) Average effective subcarrier-domain sparse representation approach for target information estimation in CP-OFDM-based passive bistatic radar. *EURASIP Journal on Advances in Signal Processing* **9**, 1–15.
19. **Anitori L, Maleki A, Otten M, Baraniuk RG and Hoogeboom P** (2013) Design and analysis of compressed sensing radar detectors. *IEEE Transactions on Signal Processing* **61**, 813–827.
20. **Wen J, Zhou Z, Li D and Tang X** (2017) A novel sufficient condition for generalized orthogonal matching pursuit. *IEEE Communications Letters* **21**, 805–808.
21. **Khanna S and Murthy CR** (2017) Decentralized joint-sparse signal recovery: A sparse Bayesian learning approach. *IEEE Transactions on Signal and Information Processing Over Networks* **3**, 29–45.
22. **Kamilov US and Mansour H** (2016) Learning optimal nonlinearities for iterative thresholding algorithms. *IEEE Signal Processing Letters* **23**, 747–751.
23. **Borgerding M, Schniter P and Rangan S** (2017) AMP-inspired deep networks for sparse linear inverse problems. *IEEE Transactions on Signal Processing* **65**, 4293–4308.
24. **Shentu X, Lai X, Wang T and Cao J** (2023) Efficient ADMM-based algorithm for regularized minimax approximation. *IEEE Signal Processing Letters* **30**, 210–214.
25. **Arjoune Y, Kaabouch N, El Ghazi H and Tamtaoui A** (2017) Compressive sensing: Performance comparison of sparse recovery algorithms. In *IEEE 7th Annual Computing and Communication Workshop and Conference (CCWC)*. Las Vegas, NV, USA. pp. 1–7.
26. **Monga V, Li Y and Eldar YC** (2021) Algorithm unrolling: Interpretable, efficient deep learning for signal and image processing. *IEEE Signal Processing Magazine* **38**, 18–44.
27. **Chen T, Chen X, Chen W, Heaton H, Liu J, Wang Z and Yin W** (2022) Learning to optimize: A primer and a benchmark. *Journal of Machine Learning Research (JMLR)* **23**, 1–59.
28. **Shlezinger N, Whang J, Eldar YC and Dimakis AG** (2023) Model-based deep learning. *Proceedings of the IEEE* **111**, 465–499.
29. **Yang Y, Sun J, Li H and Xu Z** (2020) ADMM-CSNet: A deep learning approach for image compressive sensing. *IEEE Transactions on Pattern Analysis and Machine Intelligence (TPAMI)* **42**, 521–538.
30. **Li M, Wu J, Huo W, Jiang R, Li Z, Yang J and Li H** (2022) Target-oriented SAR imaging for SCR improvement via deep MF-ADMM-Net. *IEEE Transactions on Geoscience and Remote Sensing* **60**, 1–14.
31. **Qian K, Wang Y, Jung P, Shi Y and Zhu X** (2024) HyperLISTA-ABT: An ultralight unfolded network for accurate multicomponent differential tomographic SAR inversion. *IEEE Transactions on Geoscience and Remote Sensing* **62**, 1–15.
32. **Kang L, Sun T, Luo Y, Ni J and Zhang Q** (2022) SAR imaging based on deep unfolded network with approximated observation. *IEEE Transactions on Geoscience and Remote Sensing* **60**, 1–14.
33. **Wei S, Liang J, Wang M, Shi J, Zhang X and Ran J** (2022) AF-AMPNet: A deep learning approach for sparse aperture ISAR imaging and autofocusing. *IEEE Transactions on Geoscience and Remote Sensing* **60**, 1–14.
34. **Wang M, Wei S, Liang J, Liu S, Shi J and Zhang X** (2022) Lightweight FISTA-inspired sparse reconstruction network for mmW 3-D holography. *IEEE Transactions on Geoscience and Remote Sensing.* **60**, 1–20.
35. **Zhao Z, Cao Y, Wang Y and Zhou H** (2023) Transmitted-signal-free target information extraction for OFDM-based passive radar with time-varying sparse model. *IEEE Geoscience and Remote Sensing Letters* **20**, 1–5.
36. **Hieu NQ, Hoang DT, Nguyen DN and Alsheikh MA** (2024) Reconstructing human pose from inertial measurements: a generative model-based compressive sensing approach. *IEEE Journal on Selected Areas in Communications* **42**, 2674–2687.

https://doi.org/10.1017/S1759078726103377 Published online by Cambridge University Press

37. **Creswell A, White T, Dumoulin V, Arulkumaran K, Sengupta B and Bharath AA** (2018) Generative adversarial networks: an overview. *IEEE Signal Processing Magazine* **35**, 53–65.
38. **Muller M, Picone D, Demir B, Camps-Valls G, Dalla Mura M, Ulfarsson M and Benediktsson J** (2025) Hybrid deep learning models for remote sensing image processing. *Proceedings of the IEEE*, 1–21.
39. **Liu Y, Wang D, Yang H and Li Z** (2025) A lightweight GAN-based framework for block-based compressed sensing. In *2025 17th International Conference Communication Software and Networks (ICCSN)*, Qingdao, China, pp. 127–131.
40. **Hand P and Voroninski V** (2020) Global guarantees for enforcing deep generative priors by empirical risk. *IEEE Transactions on Information Theory* **66**, 401–418.
41. **Poullin D** (2005) Passive detection using digital broadcasters (DAB, DVB) with COFDM modulation. *IEE Proceedings – Radar, Sonar and Navigation* **152**, 143–152.
42. **Wojaczek P, Cristallini D, Schell J, O'Hagan D and Summers A** (2020) Polarimetric antenna diversity for improved reference signal estimation for airborne passive radar *2020 IEEE Radar Conference (RadarConf20)*, Florence, Italy, pp. 1–6.
43. **Mao X, Li Q, Xie H, Lau RYK, Wang Z and Smolley SP** (2017) Least squares generative adversarial networks. In *2017 IEEE International Conference on Computer Vision (ICCV)*, Venice, Italy, pp. 2813–2821.
44. **Dhar M, Grover A and Ermon S** (2018) Modeling sparse deviations for compressed sensing using generative models. In *Proceedings of the 35th International Conference on Machine Learning (PMLR 80)*, Stockholm, Sweden, pp. 1214–1223.
45. **Kulpa K and Czekala Z** (2005) Masking effect and its removal in PCL radar. *IEE Proceedings – Radar, Sonar and Navigation* **152**, 174–178.
46. **Lellouch G, Mishra AK and Inggs M** (2016) Design of OFDM radar pulses using genetic algorithm based techniques. *IEEE Transactions on Aerospace and Electronic Systems* **52**, 1953–1966.



Zhixin Zhao received the B.E. and Ph.D. degrees from Wuhan University, China, in 2008 and 2013, respectively. Since 2013, she has been working with the School of Information Engineering, Nanchang University, where she is currently an Associate Professor. From December 2024 to December 2025, she was a visiting scholar with Microwave Integrated Systems Laboratory (MISL), School of Electronic, Electrical and Systems Engineering, University of Birmingham, Birmingham, UK. Her main research interests include over-the-horizon radar, passive radar signal processing, and the application of deep learning in radar signal processing.



Baiming Liang was born in 2002 and is currently pursuing a bachelor's degree in Communication Engineering at the School of Information Engineering, Nanchang University. His main research interests include radar signal processing and the application of deep learning.



Yuanshuai Chen was born in 1999 and is currently pursuing a master's degree at the School of Information Engineering, Nanchang University. His main research interests include over-the-horizon radar, passive radar signal processing.



Huilin Zhou received the M.S. and Ph.D. degrees from Wuhan University, China, in 2002 and 2006, respectively. Since 2006, he has been working with the School of Information Engineering, Nanchang University, where he is currently a professor. His main research interests include radar systems, radar signal processing, and radar imaging.

https://doi.org/10.1017/S1759078726103377 Published online by Cambridge University Press